



**HAL**  
open science

## A combined experimental and theoretical study of the lowest-lying valence, Rydberg and ionic electronic states of 2,4,6-trichloroanisole

S. Kumar, Denis Duflot, S.V. Hoffmann, N.C. Jones, P. Bolognesi, L. Carlini, R. Richter, L. Avaldi, M.J. Brunger, P. Limão-Vieira

### ► To cite this version:

S. Kumar, Denis Duflot, S.V. Hoffmann, N.C. Jones, P. Bolognesi, et al.. A combined experimental and theoretical study of the lowest-lying valence, Rydberg and ionic electronic states of 2,4,6-trichloroanisole. *Journal of Quantitative Spectroscopy and Radiative Transfer*, 2021, 271, pp.107751. 10.1016/j.jqsrt.2021.107751 . hal-03329860

**HAL Id: hal-03329860**

**<https://hal.science/hal-03329860>**

Submitted on 13 Jun 2023

**HAL** is a multi-disciplinary open access archive for the deposit and dissemination of scientific research documents, whether they are published or not. The documents may come from teaching and research institutions in France or abroad, or from public or private research centers.

L'archive ouverte pluridisciplinaire **HAL**, est destinée au dépôt et à la diffusion de documents scientifiques de niveau recherche, publiés ou non, émanant des établissements d'enseignement et de recherche français ou étrangers, des laboratoires publics ou privés.



Distributed under a Creative Commons Attribution - NonCommercial 4.0 International License

# A combined experimental and theoretical study of the lowest-lying valence, Rydberg and ionic electronic states of 2,4,6-trichloroanisole

S. Kumar <sup>a</sup>, D. Dufлот <sup>b,c,\*</sup>, S. V. Hoffmann <sup>d</sup>, N. C. Jones <sup>d</sup>, P. Bolognesi <sup>e</sup>, L. Carlini <sup>e</sup>,  
R. Richter <sup>f</sup>, L. Avaldi <sup>e</sup>, M. J. Brunger <sup>g,h</sup>, and P. Limão-Vieira <sup>a,\*</sup>

<sup>a</sup> Atomic and Molecular Collisions Laboratory, CEFITEC, Department of Physics, Universidade NOVA de Lisboa, 2829-516 Caparica, Portugal

<sup>b</sup> UMR 8523 - Physique des Lasers Atomes et Molécules, Univ. Lille, F-59000 Lille, France

<sup>c</sup> CNRS, UMR 8523, F-59000 Lille, France

<sup>d</sup> ISA, Department of Physics and Astronomy, Aarhus University, Ny Munkegade 120, DK-8000, Aarhus C, Denmark

<sup>e</sup> CNR-Istituto di Struttura della Materia, Area della Ricerca di Roma 1, 00015 Monterotondo (Roma), Italy

<sup>f</sup> Elettra-Sincrotrone Trieste, Strada Statale 14 - km 163,5 in AREA Science Park, 34149 Basovizza (Ts), Italy

<sup>g</sup> College of Science and Engineering, Flinders University, GPO Box 2100, Adelaide, SA 5001, Australia

<sup>h</sup> Dept. of Actuarial Science and Applied Statistics, Faculty of Business and Information Science, UCSI University, Kuala Lumpur 56000, Malaysia

## ABSTRACT

We investigate for the first time the gas-phase lowest-lying valence, Rydberg and ionic electronic states of 2,4,6-trichloroanisole (TCA) using synchrotron radiation for photoabsorption and photoelectron spectroscopy. The high-resolution vacuum ultraviolet photoabsorption spectrum, in the 4.0–10.8 eV energy-range, has been measured with absolute photoabsorption cross-sections and, thanks to novel *ab initio* calculations of the vertical energies and oscillator strengths, an assignment of the electronic transitions is comprehensively reported. The assignment of weak vibrational features in the absorption bands of TCA reveal that the ring and C–Cl stretching modes are mainly active. In the photoelectron spectrum the lowest 18 ionic bands, between 8 and 30 eV, have been observed and assigned using the first set of calculated valence and outer valence vertical ionisation energies. Finally, the measured absolute photoabsorption cross sections have also been used to estimate the photolysis lifetime of TCA in the upper stratosphere (20–50 km).

**Keywords:** TCA, C<sub>7</sub>H<sub>5</sub>Cl<sub>3</sub>O, electronic excitation, vibrational excitation, Rydberg series, *ab initio* calculations, photoabsorption, photoelectron spectrum, synchrotron radiation.

\* Corresponding authors:

denis.dufлот@univ-lille.fr (Denis Dufлот); plimaovieira@fct.unl.pt (Paulo Limão-Vieira)

## 1. Introduction

2,4,6-trichloroanisole,  $C_7H_5Cl_3O$ , from now on designated by the acronym TCA, was previously identified as a chemical compound responsible for strong cork taint in wine [1–5], as well as being frequently detected in both surface and drinking water [3], producing a peculiar musty or earthy odour. With considerable economic costs to the cork and wine industries, TCA levels are traceable close to its odour threshold values of 0.1–2.0 ng/L [6], and yet Buser *et al.* [4] found in different commercial wines (both white and red varieties) concentrations from 20–370 ng/L (ppt). In wines of good quality values less than 2–8 ppt were considered acceptable. The process by which wine gets contaminated with TCA, and other related chlorinated compounds, may originate from microbial degradation of chlorophenols used in insecticides and herbicides [2], or from chlorination of lignin-related substances during the chlorine bleaching used in the processing of cork, which are later extracted into the wine, yielding the musty off-flavour [4]. In the water associated with the aforementioned chlorine bleaching, 2,4,6-trichloroanisole can be readily oxidized using ultraviolet (UV)/ $H_2O_2$  and UV/persulfate (UV/PS) systems, with a removal percentage higher than 93% [7].

TCA belongs to a category of species known as volatile organic compounds (VOC), and a comprehensive investigation of its molecular and electronic structures, from the fundamental point of view, is needed to understand its chemical reactivity. This can be achieved by using spectroscopic techniques in close combination with theoretical computation. The present work is therefore part of a wider research programme, which we initiated more than two decades ago, as a joint experimental-theoretical partnership aimed at understanding the spectroscopy of volatile organic compounds and the role their trace gases play in atmospheric chemistry and physics. The spectroscopic information on the electronic states of TCA is currently scarce, in a wide wavelength region, with no experimental information on the VUV absorption bands and their cross-section values. In addition, there is also a lack of information on its excited ionic states over a wide energy range. Gas chromatography-mass spectrometry has been used to study halogenated anisole compounds in cork stoppers [1,3,5,8–10], whilst Garcia *et al.* [11] reported on the diffuse reflectance infrared Fourier transform spectrum of TCA and Karpas and co-workers [12] have performed ion mobility spectrometry for TCA detection. Corona discharge-ion mobility spectrometry, for detection of 2,4,6-trichloroanisole, was also exploited [13,14] previously.

In this paper we report, for the first time, results from an extensive study of the spectroscopy of the electronic states of TCA, by high resolution VUV photoabsorption

spectroscopy and *ab initio* theoretical calculations of its vertical excitation energies and oscillator strengths for the neutral and electronic transitions. In addition, absolute photoabsorption cross sections in the range 4.0–10.8 eV are reported. The ionisation energies, for the lowest ionic states in the 8–30 eV energy range, are obtained by photoelectron spectroscopy and are also interrogated using different levels of theory. In the next section we provide a brief summary of the structure and properties of TCA, while in Section 3 we present details of our computational methods. In Section 4 a brief discussion of the pertinent experimental details is provided, while in Section 5 our results and their discussion are given and compared to previous literature outcomes. The absolute photoabsorption cross sections are subsequently used to calculate photolysis rates at 20–50 km altitude in the Earth's atmosphere in this section. Finally, some conclusions that can be drawn from this study are given in Section 6.

## 2. Structure and properties of TCA

In this section we give a brief summary of the electronic structure of TCA, which is relevant to interpret and assess the role of the main electronic states contributing to the features observed in our photoabsorption spectrum. The TCA molecule belongs to the  $C_s$  point group symmetry in the electronic ground state (with available symmetries  $A'$  and  $A''$ ), with its geometry calculated at two different theoretical levels (see Section 3 and they are also shown in Figs. S1 and S2 of the Supplementary Information (SI)). The calculated electronic configuration of the  $\tilde{X}^1A'$  ground state is: (a) core orbitals -  $(1a'')^2 (1a')^2 (2a')^2 (3a')^2 (4a')^2 (2a'')^2 (5a')^2 (6a')^2 (7a')^2 (3a'')^2 (8a')^2$ ; (b) inner valence orbitals -  $(4a'')^2 (9a')^2 (10a')^2 (5a'')^2 (11a')^2 (12a')^2 (13a')^2 (6a'')^2 (7a'')^2 (14a')^2$ ; (c) outer valence orbitals -  $(8a'')^2 (15a')^2 (16a')^2 (17a')^2 (9a'')^2 (18a')^2 (19a')^2 (20a')^2 (10a'')^2 (21a')^2 (11a'')^2 (22a')^2 (23a')^2 (12a'')^2 (24a')^2 (25a')^2 (26a')^2 (13a'')^2 (14a'')^2 (27a')^2 (28a')^2 (15a'')^2 (29a')^2 (16a'')^2 (30a')^2 (17a'')^2 (31a')^2 (18a'')^2 (19a'')^2 (32a')^2 (20a'')^2 (33a')^2$ . The highest occupied molecular orbital (HOMO),  $33a'$ , the second highest occupied molecular orbital (HOMO-1),  $20a''$ , and the third highest occupied molecular orbital (HOMO-2),  $32a'$ , have  $\pi$  character and may be labelled  $3\pi$ ,  $2\pi$  and  $1\pi$ , respectively, whereas the HOMO-3 orbital ( $19a''$ ) and HOMO-4 orbital ( $18a''$ ) have  $\sigma$  character, although with some contributions from the  $n_{Cl}$  and  $n_O$  orbitals, respectively. The lowest unoccupied molecular orbitals (LUMO,  $21a''$ ), (LUMO+1,  $34a'$ ), and (LUMO+2,  $41a'$ ), are mainly of  $\pi^*$  antibonding character ( $1\pi^*$ ,  $2\pi^*$  and  $3\pi^*$ , respectively). These are also shown in the SI Fig. S3.

The TCA electronic excitation bands in the photoabsorption spectrum are accompanied by a fine structure assigned to the main fundamental vibrational modes. Their energies (and wavenumbers) in the ground electronic state were adopted from Garcia et al. [11], and are 0.055 eV ( $446\text{ cm}^{-1}$ ) for  $\delta_{\text{COC}}$ , 0.071 eV ( $576\text{ cm}^{-1}$ ) for  $\delta_{\text{ring}}(\text{out-of-plane})$ , 0.101 eV ( $815\text{ cm}^{-1}$ ) for  $\nu_{\text{CCl}}$ , 0.134 eV ( $1080\text{ cm}^{-1}$ ) for  $\nu_{\text{ring}}(\text{breathing})$ , 0.157 eV ( $1265\text{ cm}^{-1}$ ) for  $\delta_{\text{CH}}$ , and 0.351 eV ( $2831\text{ cm}^{-1}$ ) for  $\nu_{\text{sym}}(\text{CH}_3)$ . Note that throughout this paper, for the assignments of the vibronic structure ( $X$ ), we will adopt the notation  $X_m^n$ , with  $m$  and  $n$  denoting the initial and final vibrational states. The four lowest lying ionisation energies, which are later needed to calculate the quantum defects associated with transitions to Rydberg orbitals, have been obtained experimentally to be at 9.08 eV, 9.38 eV, 10.63 eV and 11.09 eV (see Section 4.3).

### 3. Computational details

*Ab initio* calculations were performed to determine the excitation energies of the neutral TCA molecule (see Table 1) and the valence and outer valence vertical ionisation energies (see Table 2), using the MOLPRO package [15]. First, the ground state geometry was optimised at the MP2 and CCSD levels using Dunning's cc-pVTZ atomic basis set [16,17]. It is well known that the calculation of electronic spectra, even for small organic molecules, is a difficult task (for a recent review see ref. [18]). While the very fast TD-DFT method is known to have difficulties in describing Rydberg states [19], multi-reference methods such as the CASPT2 or CASSCF/MRCI techniques become prohibitive when a large number of Rydberg orbitals have to be included in the active space. Yet, coupled cluster methods have been shown to produce reliable excitation spectra of benzene complexes [20], and more recently in the case of toluene by Serralheiro et al. [21]. Thus, the present TCA absorption spectrum was calculated at the EOM-CCSD (equation-of-motion coupled cluster method restricted to single and double excitations) level [22]. For a description of the Rydberg excited states, the basis set was augmented at the mass centre of the molecule by the Cl diffuse functions corresponding to the aug-cc-pVTZ (1s,1p,1d,1f) [17], with an additional set of diffuse (5s5p2d) orbitals taken from Kaufmann et al. [23] (aug-cc-pVTZ+R basis set). The nature of the transition was assessed by visual inspection of the natural orbitals for each transition and the average value  $\langle r^2 \rangle$  of the electronic radial spatial extent of the cloud, and the oscillator strengths were obtained using the length gauge.

The vertical ionisation energies were also obtained using Partial Third Order (P3) propagation and Outer Valence Green Function (OVGF) calculations [24], employing the cc-

pVTZ basis sets and geometry with the Gaussian16 rev. B.01 package [25]. Additional calculations have been performed at the EOMIP-CCSD level [26–28], using the Q-Chem 4.3.0 package [29].

## 4. Experimental details

### 4.1 TCA samples

The initially solid samples used in the VUV and photoelectron measurements were purchased from Sigma-Aldrich, with a stated purity of 99%. The samples were used as delivered.

### 4.2 VUV photoabsorption

Synchrotron radiation from the ASTRID2 facility at Aarhus University, Denmark, has been used to investigate the high-resolution vacuum ultraviolet (VUV) photoabsorption spectra of TCA (see Fig. 1), which was recorded at room temperature at the AU-UV beam line. The experimental apparatus has been described in detail elsewhere [30,31], so that only a brief description will be given here. Briefly, synchrotron radiation with a resolution of  $\sim 0.08$  nm (corresponding to 3 meV at the midpoint of the energy range studied) passes through a gas cell, that is filled with TCA vapour, and a photomultiplier tube is used to measure the transmitted light intensity. The low vapour pressure of TCA necessitated measurements with the gas in a static cell, closed to both the sample inlet and pumping during sample measurement. The sample pressure is measured using a capacitance manometer (Chell CDG100D) and recorded at each data point of the spectrum, which allows for correction for any small decrease in pressure due to sample condensation during the course of measurement. For wavelengths below 210 nm (energies above 5.9 eV), a small gap between the photomultiplier and the exit window of the gas cell is evacuated to prevent any absorption by molecular oxygen in the air contributing to the spectrum. For higher wavelengths, air is allowed into this gap in order to absorb higher orders of light. The sample pressure is measured using a capacitance manometer (Chell CDG100D). To guarantee the absence of any saturation effects in the data recorded, the absorption cross-sections were conservatively measured over the pressure range 0.006–0.020 mbar, with typical attenuations of less than 40%. The synchrotron beam current was monitored throughout the collection of each spectrum and background scans were recorded with the cell evacuated. Absolute photoabsorption cross sections ( $\sigma$  in units of Mb  $\equiv 10^{-18}$  cm<sup>2</sup>) were obtained using the Beer-Lambert attenuation law:  $I_t = I_0 \exp(-n\sigma x)$ , where  $I_t$  is the radiation intensity transmitted through the gas sample,  $I_0$  is that through the evacuated cell,  $n$  the molecular number density

of the sample gas,  $\sigma$  the absolute photoabsorption cross section, and  $x$  the absorption path length (15.5 cm). To accurately determine the cross-sections, the VUV spectrum was recorded in small (5 or 10 nm) sections, with at least a 10-point overlap of the adjoining sections. The light intensity at each wavelength is kept quasi-constant through ASTRID2 operating in a “top-up” mode that compensates for the constant beam decay. To compensate for the slight intensity variations ( $\sim 3\%$ ), the incident flux is normalized to the accurately determined beam current in the storage ring. The overall accuracy of the photoabsorption cross section is estimated to be better than  $\pm 5\%$ .

### 4.3 Photoelectron spectroscopy

The photoelectron spectrum of TCA was recorded at the CiPo beamline [32] of the Elettra synchrotron facility in Trieste, Italy. The VUV radiation was monochromatized at 60 eV by a spherical grating monochromator with a resolving power of about 1000. The experimental set up in this facility has also been described previously [33]. Briefly, the spectrometer consists of a VG-220i hemispherical electron energy analyser mounted in the plane perpendicular to the direction of propagation of the photon beam linearly polarized. That spectrometer is mounted at the magic angle with respect to the electric vector, in order to cancel out any angular effect due to the asymmetry parameter of the different states. The hemispherical analyser is equipped with a 2D position sensitive detector, covering a kinetic energy range of about 10% of the analyser pass energy, and possesses an energy resolution of about 2% of the pass energy. For the present measurements, a pass energy of 5 eV was used. The sample was contained in a test tube outside the vacuum chamber, and admitted at room temperature to the interaction region via a regular gas line, producing a residual gas pressure in the chamber of about  $8 \times 10^{-7}$  mbar. The spectrum was acquired with an energy step of 20 meV and an acquisition time of 12 sec/point.

## 5. Electronic state spectroscopy: Results and Discussion

The present absolute high-resolution VUV photoabsorption cross-section of TCA from 4.0 to 10.8 eV is shown in Fig. 1, while enlarged views of the 4.0-5.1 eV and 5.1-10.8 eV regions are shown in Figs. 2 and 3, respectively. To our best knowledge, no other absorption data for TCA are present in the literature. The lowest-lying absorption band in the 4.0–5.1 eV photon energy range (see Fig. 2) is due to a valence transition coupled with ring and CH deformations, which result in excitation of the CCl and ring stretching vibrational modes (see Table 3). The electronic excitation spectrum above 7.6 eV, mainly assigned to Rydberg

transitions, displays a rich fine-structure due to the  $\nu_{\text{ring}}$ (breathing) and  $\nu_{\text{sym}}(\text{CH}_3)$  modes, with the latter dominant in the energy range 8.2–10.6 eV. In addition, the structure above 8.8 eV is largely due to the overlap of different Rydberg electronic states. To avoid congestion from the different members of the Rydberg series, and the fine structure encountered, in Fig. 3 only a few assignments have been explicitly depicted. Nonetheless, detailed information on all the relevant transitions is presented in Table 4.

The major absorption bands can be classified as molecular valence transitions of ( $\pi^* \leftarrow \pi$ ) character, Rydberg and a mixture of Rydberg series. In Table 1 the experimental results and the theoretical calculations are compared and a reasonably good level of agreement between them is observed.

Table 2 lists the calculated valence and outer valence vertical ionisation energies (*IEs*) for 2,4,6-trichloroanisole, at different levels of theory, together with the results of the present photoelectron spectrum compared with previous experimental values from the literature [34,35]. The experimental ionisation energies have been obtained from the PES spectrum at the band maximum value. A close inspection of those tabulated values reveals that all the theoretical methods agree reasonably well with each other, while those provided by the Koopmans' theorem [36] are larger, due to its neglecting electron correlations and relaxation. Above the second ionic state, the P3 and OVGf vertical ionisation energy results are very close in value to each other while the EOMIP-CCSD method reproduces quite well both the present and Lichvanová et al. [34] experimental data.

From results for the vibrational modes of TCA in the literature, we have followed the notation adopted in the studies of Garcia et al. [11] in the following sections.

### 5.1. Valence state spectroscopy of TCA

From the calculations in Table 1, the absorption bands centred at 4.319 eV, 5.55(0) eV, 6.262 eV and 7.64(4) eV have been assigned to ( $\pi^* \leftarrow \pi$ ) transitions. The calculated wave functions show a mixing between excitations from the HOMO ( $3\pi$ ) and HOMO-1 ( $2\pi$ ) to the  $1\pi^*$  and  $2\pi^*$  MOs, and the HOMO-2 ( $1\pi$ ) to the  $2\pi^*$  MO. The calculated transition energies are overestimated by up to ~0.5 eV, when compared to the experiment. The first absorption band is reported with a maximum absolute cross section of 2.90 Mb, whereas the second has a maximum of 28.11 Mb (Table 1) and the third of magnitude 166.87 Mb. In comparison with the second and third bands, the one at 7.64(4) eV shows a weaker cross-section value of 18.04 Mb and a calculated oscillator strength  $f_L \approx 0.035$ . Finally, the VUV spectrum reveals another broad band at 8.837 eV which is tentatively assigned to the  $3d\sigma(\text{a}''') \leftarrow \sigma/\text{nCl}(19\text{a}'') + 4s\sigma(\text{a}')$

$\leftarrow \sigma/n_{\text{Cl}}(31a')$  transitions (see Table 1). Pure Rydberg transitions (see Table 7) in this energy range are discussed later in section 5.5.

## 5.2 Valence and vibronic excitation in the range 4.0–5.1 eV

The lowest-lying excited state of TCA, peaking at 4.319 eV (see Fig. 2), is assigned to the  $2\pi^*(34a') \leftarrow 2\pi(20a'') + 1\pi^*(21a'') \leftarrow 3\pi(33a')$  ( $1^1A'' \leftarrow \tilde{X}^1A'$ ) transition (see Table 1). The  $0_0^0$  origin band is assigned at 4.319 eV (see Table 3) and shows a weak fine structure. Note that the calculated geometry of the first excited state, at the LT-DF-LCC2 level with the cc-pVTZ basis set (see SI Fig. S4), mainly reveals the elongation of C–Cl and C–C–C bond lengths by ~41% and ~36%, respectively, from those of the ground state geometry (see Figs. S1 and S2). The geometry of this excited state is consistent with that of the anion, reported by Asfandiarov et al. [37], at the B3LYP/6-31G\* level of theory. Such a structural resemblance confirms that the captured electron in the anion is located at the LUMO, i.e. (21a''). Thus, we have calculated the different harmonic frequencies of the TCA anion and reported them in Table S1. This information proved to be very helpful in assigning the weak fine structure found in this absorption band, which is due to several modes (see Table 3 for the proposed detailed assignments), with the main contributions being from the  $\delta_{\text{ring}}(\text{out-of-plane})$ ,  $\nu_{\text{CCl}}$ ,  $\nu_{\text{ring}}(\text{breathing})$  and  $\delta_{\text{CH}}$  vibrational modes. Finally, the feature observed below the  $0_0^0$  transition is tentatively assigned to a hot-band of the C–Cl stretching mode,  $\nu_{\text{CCl}}$ .

## 5.3 Valence and vibronic excitation in the range 5.0–10.8 eV

The measured photoabsorption spectrum is presented in Fig. 3, with our proposed assignments summarized in Tables 1 and 4. The present calculations show that this energy region is mainly characterized by valence transitions, yet also with a contribution from Rydberg transitions (see Section 5.5). The lowest-lying vertical excited state of TCA in this energy region is at 5.55(0) eV and has been assigned to the  $1\pi^*(21a'') \leftarrow 2\pi(20a'') + 2\pi^*(34a') \leftarrow 3\pi(33a')$  ( $2^1A' \leftarrow \tilde{X}^1A'$ ) transition, with a calculated oscillator strength of 0.0084 (see Table 1). The next most intense absorption feature, with the  $0_0^0$  origin at 6.262 eV (see Table 1), is assigned to the  $1\pi^*(21a'') \leftarrow 2\pi(20a'') + 2\pi^*(34a') \leftarrow 3\pi(33a')$  ( $5^1A' \leftarrow \tilde{X}^1A'$ ) and  $2\pi^*(34a') \leftarrow 2\pi(20a'') + 1\pi^*(21a'') \leftarrow 3\pi(33a')$  ( $3^1A'' \leftarrow \tilde{X}^1A'$ ) transitions. Here we find calculated oscillator strengths of 0.7545 and 0.5148 (Table 1), respectively. Two other  $2\pi^*(34a') \leftarrow 1\pi(32a')$  ( $16^1A' \leftarrow \tilde{X}^1A'$ ) and  $4d\sigma(a'') \leftarrow \sigma/n_{\text{Cl}}(19a'') + 4s\sigma(a') \leftarrow \sigma/n_{\text{Cl}}(31a')$  ( $21^1A' \leftarrow \tilde{X}^1A'$ ) transitions at 7.64(4) and 8.837 eV are additionally observed. Their measured

peak cross-section values are 18.04 Mb and 104.36 Mb, respectively. The predominance of the latter is due to the first member of the Rydberg series (4s), with an estimated quantum defect of 1.70, converging to the ionisation limit ( $31a'^{-1}$ ). It also shows a fine structure superimposed on a diffuse background, due to the predissociative character of that absorption band. This band additionally shows a contribution from the  $\nu_{\text{ring}}$ (breathing) mode, with an average spacing of 0.110 eV ( $890\text{ cm}^{-1}$ ), together with contributions from the  $\text{CH}_3$  stretching modes, with an average spacing of 0.249 eV ( $2012\text{ cm}^{-1}$ ) (see Table 4). Note that Table 4 also proposes an alternative assignment being due to the  $\nu_{\text{ring}}$ (breathing) and  $\nu_{\text{CCl}}$  modes with ground state values of 0.123 eV ( $988\text{ cm}^{-1}$ ) and 0.101 eV ( $815\text{ cm}^{-1}$ ), respectively [11]. Such a difference is not significant given the broad nature of the nearby 9.308 eV feature (see Fig. 3), as well as the expected proximity of the upper electronic excited states. Additionally, a close inspection of the electron spin densities in Fig. S3 reveals the associated  $\sigma/\text{nCl}$  nature of the HOMO-3 ( $19a''$ ) and the HOMO-5 ( $31a'$ ).

Another interesting aspect of the absorption band in the 5.0–10.8 eV range pertains to the possible role of the progressions involving the  $\text{CH}_3$  stretching mode, which contribute to the underlying signal. The average excited state frequency of this stretching mode, as derived from the progressions reported in Table 4, is 0.251 eV (see Fig. 3). This is consistent with the MOs delocalized on the  $\text{CH}_3$  group shown in Fig. S1.

Finally, this energy region exhibits evidence for transitions to Rydberg states (see Section 5.5 and Table 7), converging to the ionic electronic ground ( $33a'^{-1}$ ), first ( $20a''^{-1}$ ), second ( $32a'^{-1}$ ) and third ( $19a''^{-1}$ ) excited states of TCA, and also shows some excited quanta of mainly the  $\nu_{\text{ring}}$ (breathing) and  $\nu_{\text{CH}_3}$  modes (see Tables 4 and 7).

## 5.4 Photoelectron results

The present photoelectron spectrum was measured in steps of 20 meV in the binding energy region 8.0 to 30.0 eV (see Fig. 4), with the experimental and calculated vertical ionisation energies being listed in Table 2. A previous He(I) photoelectron spectrum of 2,4,6-trichloroanisole was reported by Lichvanová et al. [34], in the energy region from 8 to 17 eV and accompanied by OVGf quantum chemical calculations. Apart from the higher energy resolution in the present experiment, which is noticeable by the fine structure assigned for the first time in Tables 5 and 6, we note a considerable discrepancy between the relative intensities of the two measurements between the 8–10 eV and the 10–12 eV ionic bands, as well as a continuous background enhancement above 12 eV in the earlier spectrum which is not visible in Fig. 4. Note that the relative intensities of the different features in the

photoelectron spectra change depending on the photon energy, and in this case the two available spectra have been measured at quite different photon energies, 60 eV and 21.22 eV, for the present study and Ref. [34], respectively.

The first and second bands, corresponding to the ionic electronic ground and first excited states of TCA, are shown in Fig. 5. These bands are assigned to ionisation from the least bound C=C  $3\pi$  (HOMO) and  $2\pi$  (HOMO-1) orbitals,  $33a'$  and  $20a''$ , although the former also have contributions from the C–O–C  $\pi$  orbitals. The first  $0_0^0$  origin band is considered to begin at 8.63(9) eV and peaking at 9.08 eV, while the second  $0_0^0$  band is tentatively placed at 9.38 eV, which is also the vertical ionisation energy value (see Table 2). Energy positions and proposed vibrational assignments of the observed features are given in Table 5. These are mainly due to contributions of the  $\delta_{\text{COC}}$  and  $\delta_{\text{ring}}(\text{out-of-plane})$  vibrational modes, with mean spacings of 0.040 and 0.060 eV, compared to 0.055 and 0.071 eV for the neutral ground state, respectively [11].

The intense third band (see Fig. 6) is considered to be due to the ionisation from the  $19a''$  orbital (HOMO-3), with  $\sigma$ ,  $n_{\text{Cl}}$  character, while the fourth band results from electron removal from the  $32a'$  orbital (HOMO-2) with  $\pi$ -ring character (see Fig. S3). These bands have vertical ionisation energies of 10.63 eV and 11.09 eV, and their order appears reversed in Table 2. The weak fine structure in these bands is tentatively assigned to the  $\nu_{\text{ring}}(\text{breathing})$  and  $\delta_{\text{COC}}$  vibrational modes, and the  $\delta_{\text{ring}}(\text{out-of-plane})$  vibrational modes with mean energies of 0.100 eV and 0.040 eV, and 0.060 eV, respectively (see Table 6). Despite the apparently similar observed vibrational excitation energy, we also assign the relevant band structure to be due to ring stretching (breathing) from  $\nu_{\text{CCl}}$  motion under the same rationale as in Sec. 5.3. This is consistent with the Rydberg character of the 8.837 eV feature in the VUV photoabsorption spectrum (see Table 7), where identical vibrational modes are expected to be activated in the lowest-lying ionic states.

The next two ionic bands have their  $0_0^0$  origins (and vertical ionisation values) at 11.41 eV and 11.74 eV (see Table 6), and are related to the ionisation of the  $31a'$  orbital (HOMO-5) and  $17a''$  orbital (HOMO-6) with  $\sigma$ ,  $n_{\text{Cl}}$  character (see Table 2 and Fig. S3). The fine structure in these bands is tentatively assigned in Table 6 to the  $\nu_{\text{ring}}(\text{breathing})/\nu_{\text{CCl}}$  and  $\delta_{\text{COC}}$  vibrational modes, the former coupled with a  $\delta_{\text{ring}}(\text{out-of-plane})$  mode.

Water, present as a minor contaminant, was used to calibrate the photoelectron energy spectrum at 12.62 eV, and so no attempts were made to assign any fine structure for photon energies above that value as they may also contain contributions from relevant H<sub>2</sub>O ionic

states [38]. In order to assign the lowest lying Rydberg members of TCA, converging to the ionic electronic ground ( $33a'^{-1}$ ), first ( $20a''^{-1}$ ), second ( $32a'^{-1}$ ) and third ( $19a''^{-1}$ ) excited states, we have used the experimental vertical ionisation energy (IE) values of 9.08 eV, 9.38 eV, 11.09 eV and 10.63 eV, respectively (see Table 2).

## 5.5 Rydberg transitions

The VUV photoabsorption spectrum above 5.5 eV consists of a few structures, superimposed on a diffuse absorption feature extending to the lowest ionisation energies, which are here reported for the first time. The experimental ionisation energy values from the photoelectron spectrum in Table 2 are used to describe those Rydberg series, with the proposed Rydberg structures being listed in Table 7. Note that the observed peak positions have been tested using the Rydberg formula:  $E_n = E_i - R / (n - \delta)^2$ , where  $E_i$  is the ionisation energy,  $n$  is the principal quantum number of the Rydberg orbital of energy  $E_n$ ,  $R$  is the Rydberg constant (13.61 eV), and  $\delta$  the quantum defect resulting from the penetration of the Rydberg orbital into the core.

The lowest transition energy is tentatively assigned to a 4s state at 5.55(0) eV for the Rydberg series converging to the ionic electronic ground state ( $33a'^{-1}$ ), with a quantum defect  $\delta = 2.04$  (see Table 7). Note that higher members of this Rydberg series are proposed to extend to  $n = 6$ . The first members of the np and nd series are associated with the peaks at 6.262 eV ( $\delta = 1.80$ ) and 7.64(4) eV ( $\delta = -0.08$ ), respectively (see again Table 7).

The first members of the ns, np, and nd series converging to the ionic electronic first excited state of TCA ( $20a''^{-1}$ ), are associated with the peaks at 6.262 eV ( $\delta = 1.91$ ) and 7.64(4) eV ( $\delta = 1.19$  and  $\delta = 0.19$ ), respectively (see Table 7). Note that these Rydberg transitions (see Figure 3) are accompanied by a vibronic structure, which is proposed to be mainly due to  $\nu_{\text{CH}_3}$  progressions with an average spacing of 0.254 eV (see Table 4). The higher members of the np Rydberg series are proposed to extend to  $n = 7$ .

As far as the members of the Rydberg series converging to the ionic electronic second excited state ( $32a'^{-1}$ ) are concerned, the  $n = 4$  states for ns, np and the  $n = 3$  state for nd are considered to be at 7.64(4) eV, 8.46(9) eV and 9.42(9) eV, respectively (see Table 7) with quantum defects of 2.01, 1.72 and 0.13, respectively. Some of the fine structure here has been assigned to vibrational excitation involving  $\nu_{\text{CH}_3}$  progressions,  $\nu_{\text{ring}}(\text{breathing})/\nu_{\text{CCl}}$  and combinations of these modes (see Tables 4 and 7).

Regarding the Rydberg series converging to the ionic electronic third excited state ( $19a''^{-1}$ ), the lowest-lying members have been assigned to the 4s, 4p and 3d states at 7.64(4)

eV, 8.837 eV and 8.93(3) eV, with quantum defects  $\delta = 1.86, 1.24$  and  $0.17$ , respectively, and accompanied by vibronic structure which is tentatively attributed to  $\nu_{\text{CH}_3}$  progressions (see Table 4). Note that the 4p feature is, according to the theoretical calculations in Table 1, also assigned to the  $3d\sigma(a'') \leftarrow \sigma/n_{\text{Cl}}(19a'') + 4s\sigma(a') \leftarrow \sigma/n_{\text{Cl}}(31a')$  transitions, although the obtained quantum defect does not resemble any of the  $4s\sigma$  and/or  $3d\sigma$  Rydberg members.

The higher-order members of these Rydberg series, for which the relative intensity decreases, are difficult to assign due to overlap with other transitions and possible vibronic structure. We have thus not made any attempt to identify those higher members of the Rydberg series, due to the broad and structureless nature of the absorption bands. Note that the clear increase in the absorption intensity in the range above  $\sim 7.5$  eV, may be related to low-lying pre-dissociative or dissociative excited neutral states.

## 5.6 Absolute photoabsorption cross sections and atmospheric photolysis

The present optical measurements were carried out in the pressure range 0.006–0.020 mbar, and they revealed no evidence for changes in the absolute cross sections or peak energies as a function of pressure. Thus the present spectra are free of any saturation effects. A literature survey reveals no other previous photoabsorption cross sections of TCA in the 4.0 – 10.8 eV photon energy range to compare with. However, the agreement of previous cross sections measured at the AU-UV beam line of the ASTRID2 synchrotron facility at Aarhus University, see e.g. [39–41], with the most precise corresponding data available in the literature (see Eden *et al.* [30] and references therein), indicates that our adopted procedures do not suffer from systematic errors. Hence the present TCA cross sections can be relied upon across the energy range studied (4.0–10.8 eV).

The present absolute cross sections below 6.89 eV (i.e. above 180 nm) can be used in combination with solar actinic flux [42] measurements, from the literature, to estimate the photolysis rate of TCA in the atmosphere from an altitude close to the ground to the stratopause at 50 km. Details of the calculation procedure are presented in ref. [43], in which the quantum yield for dissociation following absorption is assumed to be unity. Note that the reciprocal of the photolysis rate at a given altitude corresponds to the local photolysis lifetime. Photolysis lifetimes of less than 3 hours sunlit day were calculated at altitudes above 20 km. This shows that TCA molecules can be broken up quite efficiently by UV absorption at those altitudes. From the ground level up to the tropopause the calculated lifetimes are also considered to be negligible. We are not aware of any gas-phase reactions between TCA and available atmospheric radicals that may present relevant sink mechanisms. There have, to the

best of our knowledge, not been any quantitative studies as to the atmospheric abundance of TCA as a function of altitude. It is, however, only likely to be a trace species, although we highlight that trace species can play very important roles in atmospheric chemistry and in the role of electron- and photon-driven atmospheric behaviour (see e.g. [44,45] on NO). However, in reactions with ozone and  $\cdot\text{OH}$  radicals formed upon ozone decomposition from drinking water treatment, for disinfection and oxidation of micropollutants, Peter and von Gunten [44] found rate constants of  $9.47 \times 10^{-23} \text{ cm}^3 \text{ molecules}^{-1} \text{ s}^{-1}$  and  $8.47 \times 10^{-12} \text{ cm}^3 \text{ molecules}^{-1} \text{ s}^{-1}$ , respectively, the former being negligible relative to the latter [46]. Given that TCA can easily undergo photolysis at very low altitudes, reactions with ozone may be expected in the troposphere. However, they will be governed under local climate conditions, in particular in urban areas with high levels of vehicle emissions and very warm weather. Reactions with  $\cdot\text{OH}$  radicals are perhaps more plausible, and these may provide a main reactive sink mechanism in the troposphere in strong competition with solar photolysis. However, these are but conjectures at this time with a comprehensive investigation of the gas-phase reactions between TCA and key selected environmental radicals being needed to clarify the role of those mechanisms and to obtain the related rate constants.

## 6. Conclusion

The present work provides the first complete study to date of the VUV electronic spectroscopy of TCA, and gives the most reliable set of absolute photoabsorption cross sections between 4.0 to 10.8 eV. The observed low energy structure has been assigned to valence, Rydberg and mixed valence/Rydberg transitions, on the basis of comparisons with *ab initio* calculations of the vertical excitation energies and oscillator strengths for this molecule. The theoretical results were found to be in reasonably good agreement with the experiments, predicting significant valence, Rydberg and mixing valence/Rydberg with  $\pi^*$  states. The main absorption bands have been assigned to the  $2\pi^*(34a') \leftarrow 2\pi(20a'') + 1\pi^*(21a'') \leftarrow 3\pi(33a')$  ( $1^1A'' \leftarrow \tilde{X}^1A'$ ),  $1\pi^*(21a'') \leftarrow 2\pi(20a'') + 2\pi^*(34a') \leftarrow 3\pi(33a')$  ( $2^1A' \leftarrow \tilde{X}^1A'$ ),  $1\pi^*(21a'') \leftarrow 2\pi(20a'') + 2\pi^*(34a') \leftarrow 3\pi(33a')$  ( $5^1A' \leftarrow \tilde{X}^1A'$ ) /  $2\pi^*(34a') \leftarrow 2\pi(20a'') + 1\pi^*(21a'') \leftarrow 3\pi(33a')$  ( $3^1A'' \leftarrow \tilde{X}^1A'$ ),  $2\pi^*(34a') \leftarrow 1\pi(32a')$  ( $16^1A' \leftarrow \tilde{X}^1A'$ ) and  $3d\sigma(a'') \leftarrow \sigma/\text{nCl}(19a'') + 4s\sigma(a') \leftarrow \sigma/\text{nCl}(31a')$  ( $21^1A' \leftarrow \tilde{X}^1A'$ ) transitions. An analysis of the observed vibronic structure in the photoabsorption spectra was performed for the first time, and those structures were mainly assigned to the  $\delta_{\text{COC}}$ ,  $\delta_{\text{ring}}(\text{out-of-plane})$ ,  $\nu_{\text{Cl}}$ ,  $\nu_{\text{ring}}(\text{breathing})$ , and  $\nu_{\text{sym}}(\text{CH}_3)$  modes. Moreover, the present photoelectron spectrum was obtained in a wide binding energy

range from 8 eV up to 30 eV, where fine structure in the lowest-lying ionic bands (up to 12 eV) were assigned to the active modes. The photolysis lifetimes of TCA have also been carefully derived for the Earth's troposphere and stratosphere, and indicated that solar photolysis may represent an important sink mechanism for TCA in the terrestrial atmosphere.

## **Notes**

The authors declare no competing financial interest.

## **Author contributions**

S.K., N.C.J, S.V.H, P.L.-V.: data acquisition experiment, data analysis; D.D.: quantum chemical calculations; P.B., L.C., R.R., L.A.: photoelectron data acquisition and data analysis; D.D., N.C.J, S.V.H, M.J.B. and P.L.-V.: interpretation of the data and manuscript preparation.

## **Declaration of Competing Interest**

The authors declare that they have no known competing financial interests or personal relationships that could have appeared to influence the work reported in this paper.

## **Acknowledgments**

SK acknowledges the Portuguese National Funding Agency FCT through the Grant PD/BD/142831/2018 and together with PLV the Research Grants CEFITEC (UIDB/00068/2020) and PTDC/FIS-AQM/31281/2017. This work was also supported by the Radiation Biology and Biophysics Doctoral Training Programme (RaBBiT; Grant PD/00193/2012) and UCIBIO (Grant UIDB/04378/2020). DD acknowledges the support of the OVERSEE and CAPPa grants, managed by the Agence Nationale de la Recherche under the frame programs Investissements d'Avenir ANR-10-LABX-005 and I-SITE ULNE/ANR-16-IDEX-0004 ULNE, respectively. D.D. also thanks the Région Hauts de France, the Ministre de l'Enseignement Supérieur et de la Recherche (CPER Climibio) and the European Fund for Regional Economic Development for their support. This work used HPC resources from GENCI-TGCC (Grant No. 2020-A0050801859) and the Centre de Ressources Informatiques (CRI) of the Université de Lille. This contribution is based upon work from COST Action CA18212-Molecular Dynamics in the GAS phase (MD-GAS), supported by COST (European Cooperation in Science and Technology). Finally, MJB thanks the Australian Research Council for partial financial support through grant # DP180101655.

## References

- [1] Gómez-Ariza JL, García-Barrera T, Lorenzo F. Optimisation of a two-dimensional on-line coupling for the determination of anisoles in wine using ECD and ICP-MS after SPME-GC separation. *J Anal At Spectrom* 2005;20:883–8. <https://doi.org/10.1039/b505003k>.
- [2] Callejón RM, Ubeda C, Ríos-Reina R, Morales ML, Troncoso AM. Recent developments in the analysis of musty odour compounds in water and wine: A review. *J Chromatogr A* 2016;1428:72–85. <https://doi.org/10.1016/j.chroma.2015.09.008>.
- [3] Cacho JI, Nicolás J, Viñas P, Campillo N, Hernández-Córdoba M. Direct sample introduction-gas chromatography-mass spectrometry for the determination of haloanisole compounds in cork stoppers. *J Chromatogr A* 2016;1475:74–9. <https://doi.org/10.1016/j.chroma.2016.11.002>.
- [4] Buser H-R, Zanier C, Tanner H. Identification of 2,4,6-Trichloroanisole as a Potent Compound Causing Cork Taint in Wine. *J Agric Food Chem* 1982;30:359–62. <https://doi.org/10.1021/jf00110a037>.
- [5] Evans TJ, Butzke E, Ebeler SE. Analysis of 2,4,6-trichloroanisole in wines using solid-phase microextraction coupled to gas chromatography-mass spectrometry. *J Chromatogr A* 1997;786:293–8.
- [6] Benanou D, Acobas F, Roubin MR de. Optimization of stir bar sorptive extraction applied to the determination of pesticides in vinegars. *J Chromatogr A* 2007;1165:144–50. <https://doi.org/10.1016/j.chroma.2007.07.058>.
- [7] Zhu H, Jia R, Sun S, Feng G, Wang M, Zhao Q, et al. Elimination of trichloroanisoles by UV/H<sub>2</sub>O<sub>2</sub>: Kinetics, degradation mechanism, water matrix effects and toxicity assessment. *Chemosphere* 2019;230:258–67. <https://doi.org/10.1016/j.chemosphere.2019.05.052>.
- [8] Sadoughi N, Schmidtke LM, Antalick G, Blackman JW, Steel CC. Gas chromatography-mass spectrometry method optimized using response surface modeling for the quantitation of fungal off-flavors in grapes and wine. *J Agric Food Chem* 2015;63:2877–85. <https://doi.org/10.1021/jf505444r>.
- [9] McLellan I, Hursthouse A, Morrison C, Varela A, Pereira CS. Development of a robust chromatographic method for the detection of chlorophenols in cork oak forest soils. *Environ Monit Assess* 2014;186:1281–93. <https://doi.org/10.1007/s10661-013-3457-z>.
- [10] Slabizki P, Fischer C, Legrum C, Schmarr H-G. Characterization of Atypical Off-Flavor Compounds in Natural Cork Stoppers by Multidimensional Gas

- Chromatographic Techniques. *J Agric Food Chem* 2015;63:7840–8.  
<https://doi.org/10.1021/acs.jafc.5b02793>.
- [11] Garcia AR, Lopes LF, Barros RB De, Ilharco LM. The problem of 2,4,6-trichloroanisole in cork planks studied by attenuated total reflection infrared spectroscopy: Proof of concept. *J Agric Food Chem* 2015;63:128–35.  
<https://doi.org/10.1021/jf503309a>.
- [12] Karpas Z, Guamán A V., Calvo D, Pardo A, Marco S. The potential of ion mobility spectrometry (IMS) for detection of 2,4,6-trichloroanisole (2,4,6-TCA) in wine. *Talanta* 2012;93:200–5. <https://doi.org/10.1016/j.talanta.2012.02.012>.
- [13] Lichvanová Z, Ilbeigi V, Sabo M, Tabrizchi M, Matejčík Š. Using corona discharge-ion mobility spectrometry for detection of 2,4,6-Trichloroanisole. *Talanta* 2014;127:239–43. <https://doi.org/10.1016/j.talanta.2014.04.021>.
- [14] Márquez-Sillero I, Cárdenas S, Valcárcel M. Direct determination of 2,4,6-trichloroanisole in wines by single-drop ionic liquid microextraction coupled with multicapillary column separation and ion mobility spectrometry detection. *J Chromatogr A* 2011;1218:7574–80. <https://doi.org/10.1016/j.chroma.2011.06.032>.
- [15] Werner H-J, Knowles PJ, Knizia G, Manby FR, Schütz M, Celani P, et al. MOLPRO, version 2015.1. *Wiley Interdiscip Rev Comput Mol Sci* 2012;2:242.
- [16] Dunning TH. Gaussian basis sets for use in correlated molecular calculations. I. The atoms boron through neon and hydrogen. *J Chem Phys* 1989;90:1007–23.  
<https://doi.org/10.1063/1.470645>.
- [17] Woon DE, Dunning TH. Gaussian basis sets for use in correlated molecular calculations. III. The atoms aluminum through argon. *J Chem Phys* 1993;98:1358–71.  
<https://doi.org/10.1063/1.464303>.
- [18] Serrano-Andrés L, Merchán M. Quantum chemistry of the excited state: 2005 Overview. *J Mol Struct-Theochem* 2005;729:99–108.  
<https://doi.org/10.1016/j.theochem.2005.03.020>.
- [19] Dreuw A, Head-Gordon M. Single-reference ab initio methods for the calculation of excited states of large molecules. *Chem Rev* 2005;105:4009–37.  
<https://doi.org/10.1021/cr0505627>.
- [20] Ahnen S, Hehn AS, Vogiatzis KD, Trachsel MA, Leutwyler S, Klopper W. Accurate computations of the structures and binding energies of the imidazole ⋯benzene and pyrrole ⋯benzene complexes. *Chem Phys* 2014;441:17–22.  
<https://doi.org/10.1016/j.chemphys.2014.05.023>.

- [21] Serralheiro C, Duflot D, Da Silva FF, Hoffmann S V., Jones NC, Mason NJ, et al. Toluene Valence and Rydberg Excitations as Studied by ab initio Calculations and Vacuum Ultraviolet (VUV) Synchrotron Radiation. *J Phys Chem A* 2015;119:9059–69. <https://doi.org/10.1021/acs.jpca.5b05080>.
- [22] Hampel C, Peterson KA, Werner HJ. A comparison of the efficiency and accuracy of the quadratic configuration interaction (QCISD), coupled cluster (CCSD), and Brueckner coupled cluster (BCCD) methods. *Chem Phys Lett.* 1992;190:1–12. [https://doi.org/10.1016/0009-2614\(92\)86093-W](https://doi.org/10.1016/0009-2614(92)86093-W).
- [23] Kaufmann K, Baumeister W, Jungen M. Universal Gaussian basis sets for an optimum representation of Rydberg and continuum wavefunctions. *J Phys B At Mol Opt Phys* 1989;22:2223–40. <https://doi.org/10.1088/0953-4075/22/14/007>.
- [24] A. M. Ferreira, Seabra G, Dolgounitcheva O, Zakrzewski VG, Ortiz J V. Quantum-Mechanical Prediction of Thermochemical Data. In: Cioslowski J, editor. vol. 22, Dordrecht: Kluwer Academic; 2001, p. 131–60.
- [25] Frisch MJ, Trucks GW, Schlegel HB, Scuseria GE, Robb MA, Cheeseman JR, et al. *Gaussian 16 Rev. B.01*, Wallingford, CT 2016.
- [26] Sinha D, Mukhopadhyay SK, Chaudhuri R, Mukherjee D. The eigenvalue-independent partitioning technique in Fock space: An alternative route to open-shell coupled-cluster theory for incomplete model spaces. *Chem Phys Lett* 1989;154:544–9. [https://doi.org/10.1016/0009-2614\(89\)87149-0](https://doi.org/10.1016/0009-2614(89)87149-0).
- [27] Stanton JF, Gauss J. Analytic energy derivatives for ionized states described by the equation-of-motion coupled cluster method. *J Chem Phys* 1994;101:8938–44. <https://doi.org/10.1063/1.468022>.
- [28] Nooijen M, Bartlett RJ. Equation of motion coupled cluster method for electron attachment. *J Chem Phys* 1995;102:3629–47. <https://doi.org/10.1063/1.468592>.
- [29] Shao Y, Gan Z, Epifanovsky E, Gilbert ATB, Wormit M, Kussmann J, et al. Advances in molecular quantum chemistry contained in the Q-Chem 4 program package. *Mol Phys* 2015;113:184–215. <https://doi.org/10.1080/00268976.2014.952696>.
- [30] Eden S, Limão-Vieira P, Hoffmann S V., Mason NJ. VUV photoabsorption in CF<sub>3</sub>X (X = Cl, Br, I) fluoro-alkanes. *Chem Phys* 2006;323:313–33.
- [31] Palmer MH, Ridley T, Hoffmann SV, Jones NC, Coreno M, De Simone M, et al. Interpretation of the vacuum ultraviolet photoabsorption spectrum of iodobenzene by ab initio computations. *J Chem Phys* 2015;142:134302. <https://doi.org/10.1063/1.4916121>.

- [32] Derossi A, Lama F, Piacentini M, Prosperi T, Zema N. High flux and high resolution beamline for elliptically polarized radiation in the vacuum ultraviolet and soft x-ray regions. *Rev Sci Instrum* 1995;66:1718–20. <https://doi.org/10.1063/1.1145828>.
- [33] Plekan O, Sa H, Ciavardini A, Callegari C, Cautero G, Dri C, et al. Experimental and Theoretical Photoemission Study of Indole and Its Derivatives in the Gas Phase. *J Phys Chem A* 2020;124:4115–27. <https://doi.org/10.1021/acs.jpca.0c02719>.
- [34] Lichvanová Z, Stano M, Papp P, Matejčík Š. 23rd Europhysics Conference on Atomic and Molecular Physics of Ionized Gases. In: V. Medvecká, Papp P, Országh J, Matejčík Š, editors. 23rd Europhys. Conf. At. Mol. Phys. Ioniz. Gases, European Physical Society; 2016, p. 1–415.
- [35] Dousty F, O'Brien RT, Gahler R, Kersten H, Benter T. Carbon disulfide as a dopant in photon-induced chemical ionization mass spectrometry. *Rapid Commun Mass Spectrom* 2013;27:1969–76. <https://doi.org/10.1002/rcm.6644>.
- [36] Koopmans T. Über die Zuordnung von Wellenfunktionen und Eigenwerten zu den Einzelnen Elektronen Eines Atoms. *Physica* 1934;1:104–13. [https://doi.org/10.1016/S0031-8914\(34\)90011-2](https://doi.org/10.1016/S0031-8914(34)90011-2).
- [37] Asfandiarov NL, Muftakhov M V., Pshenichnyuk SA, Papp P, Danko M, Lacko M, et al. Dissociative electron attachment to 2,4,6-trichloroanisole and 2,4,6-tribromoanisole molecules. *J Chem Phys* 2017;147:234302. <https://doi.org/10.1063/1.5007816>.
- [38] Truong SY, Yenchu AJ, Juarez AM, Cavanagh SJ, Bolognesi P, King GC. Threshold photoelectron spectroscopy of H<sub>2</sub>O and D<sub>2</sub>O over the photon energy range 12–40 eV. *Chem Phys* 2009;355:183–93. <https://doi.org/10.1016/j.chemphys.2008.12.009>.
- [39] Limão-Vieira P, Jones NC, Hoffmann S V., Duflo D, Mendes M, Lozano AI, et al. Revisiting the photoabsorption spectrum of NH<sub>3</sub> in the 5.4–10.8 eV energy region. *J Chem Phys* 2019;151:184302. <https://doi.org/10.1063/1.5128051>.
- [40] Lange E, Jones NC, Hoffmann S V., Lozano AI, Kumar S, Homem MGP, et al. The electronic excited states of dichloromethane in the 5.8–10.8 eV energy range investigated by experimental and theoretical methods. *J Quant Spectrosc Radiat Transf* 2020;253:107172. <https://doi.org/10.1016/j.jqsrt.2020.107172>.
- [41] Lange E, Lozano AI, Jones NC, Hoffmann SV, Kumar S, Śmiałek MA, et al. Absolute Photoabsorption Cross-Sections of Methanol for Terrestrial and Astrophysical Relevance. *J Phys Chem A* 2020;124:8496–508. <https://doi.org/10.1021/acs.jpca.0c06615>.
- [42] DeMore WB, Sander SP, Golden DM, Hampson RF, Kurylo MJ, Howard CJ, et al.

- Chemical kinetics and photochemical data for use in stratospheric modeling. JPL Publ 1997;97-4:278. <https://doi.org/10.1002/kin.550171010>.
- [43] Limão-Vieira P, Eden S, Kendall PA, Mason NJ, Hoffmann S V. VUV Photo-Absorption Cross-Section for CCl<sub>2</sub>F<sub>2</sub>. Chem Phys Lett 2002;364:535-41.
- [44] Cartwright DC, Brunger MJ, Campbell L, Mojarrabi B, Teubner PJO. Nitric oxide excited under auroral conditions: Excited state densities and band emissions. J Geophys Res 2000;105:20857-67. <https://doi.org/10.1029/1999JA000333>.
- [45] Campbell L, Brunger MJ, Petrovic ZL, Jelisavcic M, Panajotovic R, Buckman SJ. Infrared auroral emissions driven by resonant electron impact excitation of NO molecules. Geophys Res Lett 2004;31:L10103. <https://doi.org/10.1029/2003GL019151>.
- [46] Peter A, Von Gunten U. Oxidation kinetics of selected taste and odor compounds during ozonation of drinking water. Environ Sci Technol 2007;41:626-31. <https://doi.org/10.1021/es061687b>.

## Figure captions

Fig. 1. The high-resolution VUV photoabsorption spectrum of TCA,  $C_7H_5Cl_3O$ , in the 4.0–10.8 eV photon energy range. See text for further details.

Fig. 2. The VUV photoabsorption spectrum of TCA,  $C_7H_5Cl_3O$ , in the 4.0–5.1 eV photon energy range. See text for details on the assignments.

Fig. 3. The VUV photoabsorption spectrum of TCA,  $C_7H_5Cl_3O$ , in the 5.0–10.8 eV photon energy range. See text for details on the assignments.

Fig. 4. The TCA,  $C_7H_5Cl_3O$ , photoelectron spectrum in the 8.0–30.0 eV binding energy range. The 12.62 eV feature is assigned to the ionisation of  $H_2O$  which is present as a contaminant. See text for further details.

Fig. 5. The first and second photoelectron bands of TCA,  $C_7H_5Cl_3O$ , which are assigned to ionisation from the least bound  $C=C$   $3\pi$  and  $2\pi$  orbitals, namely the  $33a'$  and  $20a''$  orbitals.

Fig. 6. Photoelectron bands of TCA,  $C_7H_5Cl_3O$ , in the 10.2–12.2 eV photon energy range. See text for further details.

## Table captions

Table 1. Calculated vertical excitation energies (EOM-CCSD/aug-cc-pVTZ+R basis set) and oscillator strengths (singlet states) of TCA ( $C_7H_5Cl_3O$ ), compared with results from the present experimental data (all energies in eV). See details in text.

Table 2. Calculated valence and outer valence vertical ionisation energies and intensities (cc-pVTZ basis set at OVGf, P3/P3+ and EOMIP-CCSD/cc-pVTZ levels, CCSD/cc-pVTZ geometry) and experimental binding energies of TCA,  $C_7H_5Cl_3O$ . For the sake of comparison, previous literature experimental values are also reported. All the energy values are in eV.

Table 3. Proposed vibrational assignments in the 4.0–5.0 eV absorption band of TCA,  $C_7H_5Cl_3O$ . See text for further details.

Table 4. Proposed vibrational assignments and progressions in the 8.0–10.8 eV absorption band of TCA,  $C_7H_5Cl_3O$ . See text for further details.

Table 5. Proposed vibrational assignments in the 8.0–10.0 eV photoelectron band of TCA,  $C_7H_5Cl_3O$ . See text for further details.

Table 6. Proposed vibrational assignments in the 10.2–12.2 eV photoelectron band of TCA,  $C_7H_5Cl_3O$ . See text for further details.

Table 7. Energy value (eV), quantum defect ( $\delta$ ) and assignment of the Rydberg series converging to the ionic electronic ground ( $33a'^{-1}$ ), first ( $20a''^{-1}$ ), second ( $32a'^{-1}$ ) and third ( $19a''^{-1}$ ) excited states of TCA,  $C_7H_5Cl_3O$ .

Fig. 1. The high-resolution VUV photoabsorption spectrum of TCA,  $C_7H_5Cl_3O$ , in the 4.0–10.8 eV photon energy range. See text for further details.

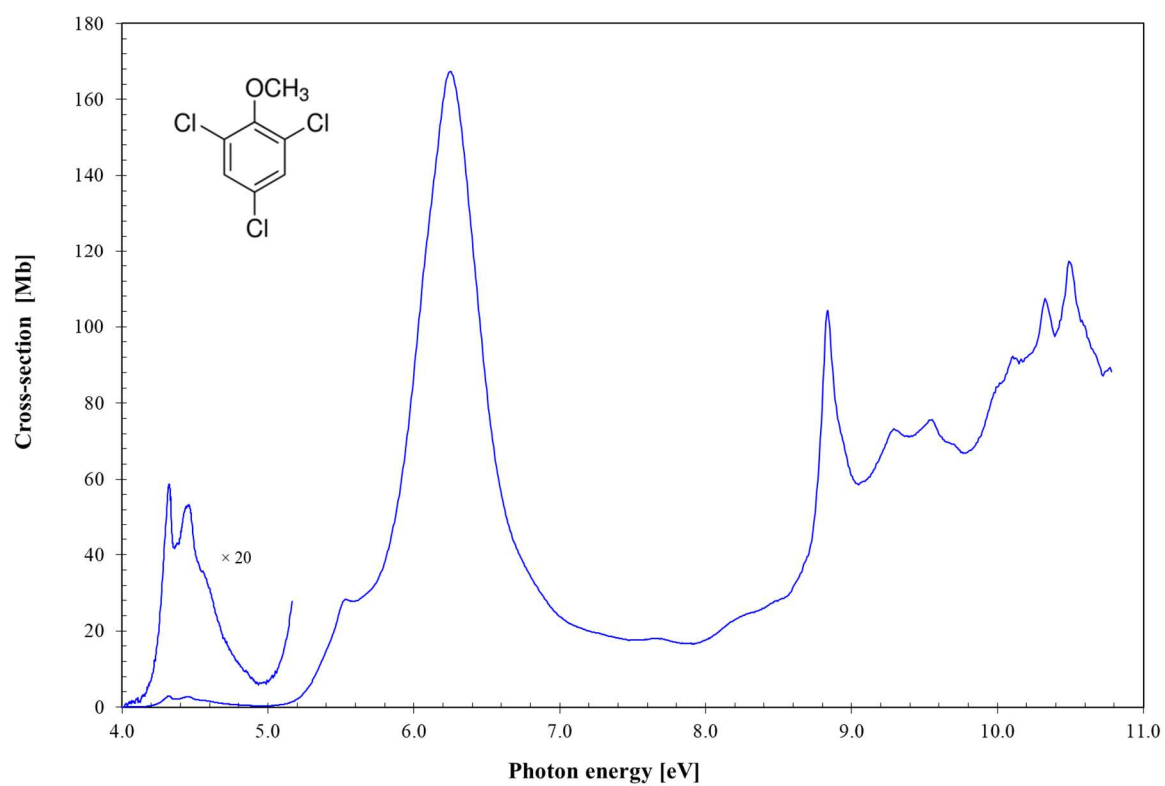


Fig. 2. The VUV photoabsorption spectrum of TCA,  $C_7H_5Cl_3O$ , in the 4.0–5.1 eV photon energy range. See text for details on the assignments.

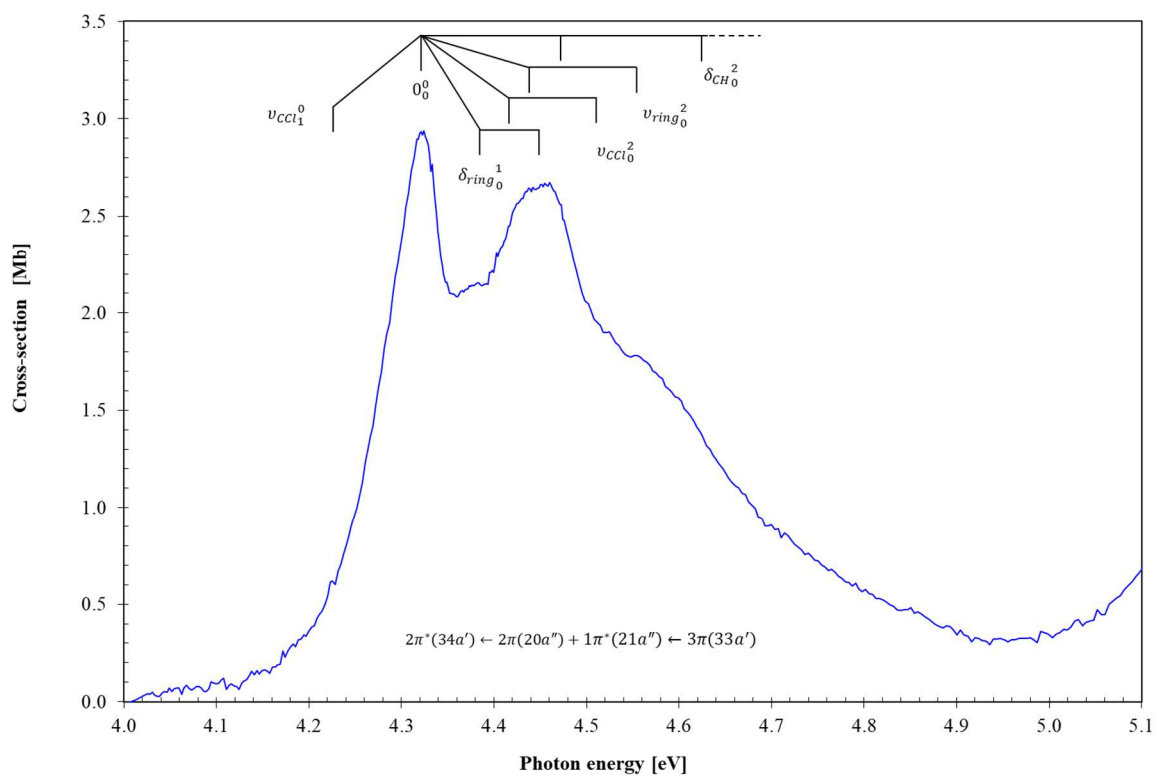


Fig. 3. The VUV photoabsorption spectrum of TCA,  $C_7H_5Cl_3O$ , in the 5.0–10.8 eV photon energy range. See text for details on the assignments.

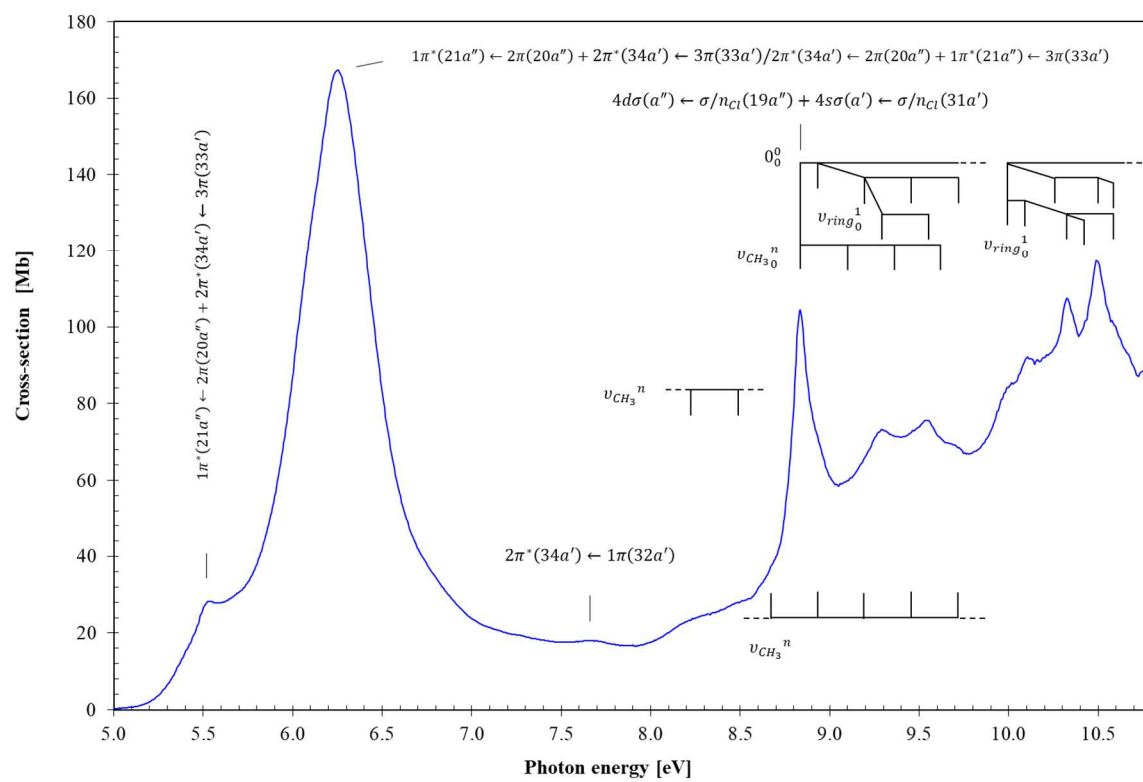


Fig. 4. The TCA,  $C_7H_5Cl_3O$ , photoelectron spectrum in the 8.0–30.0 eV binding energy range. The 12.62 eV feature is assigned to the ionisation of  $H_2O$  which is present as a contaminant. See text for further details.

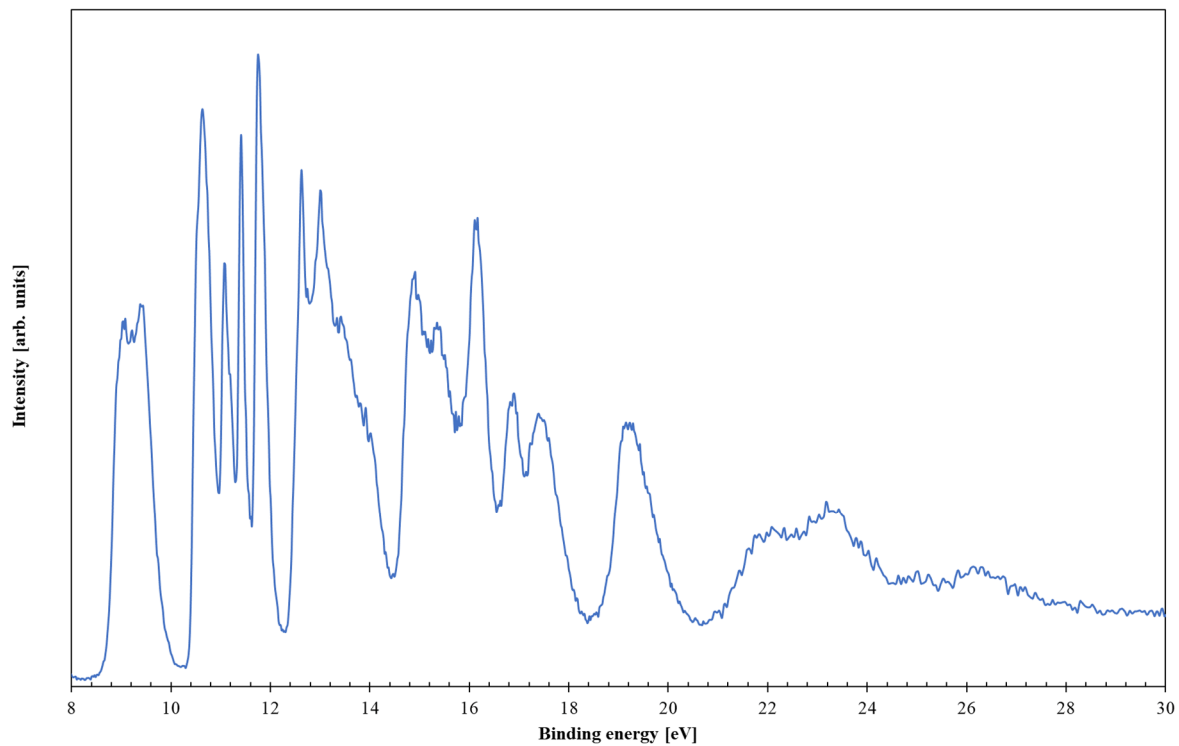


Fig. 5. The first and second photoelectron bands of TCA,  $C_7H_5Cl_3O$ , which are assigned to ionisation from the least bound C=C  $3\pi$  and  $2\pi$  orbitals, namely the  $33a'$  and  $20a''$  orbitals.

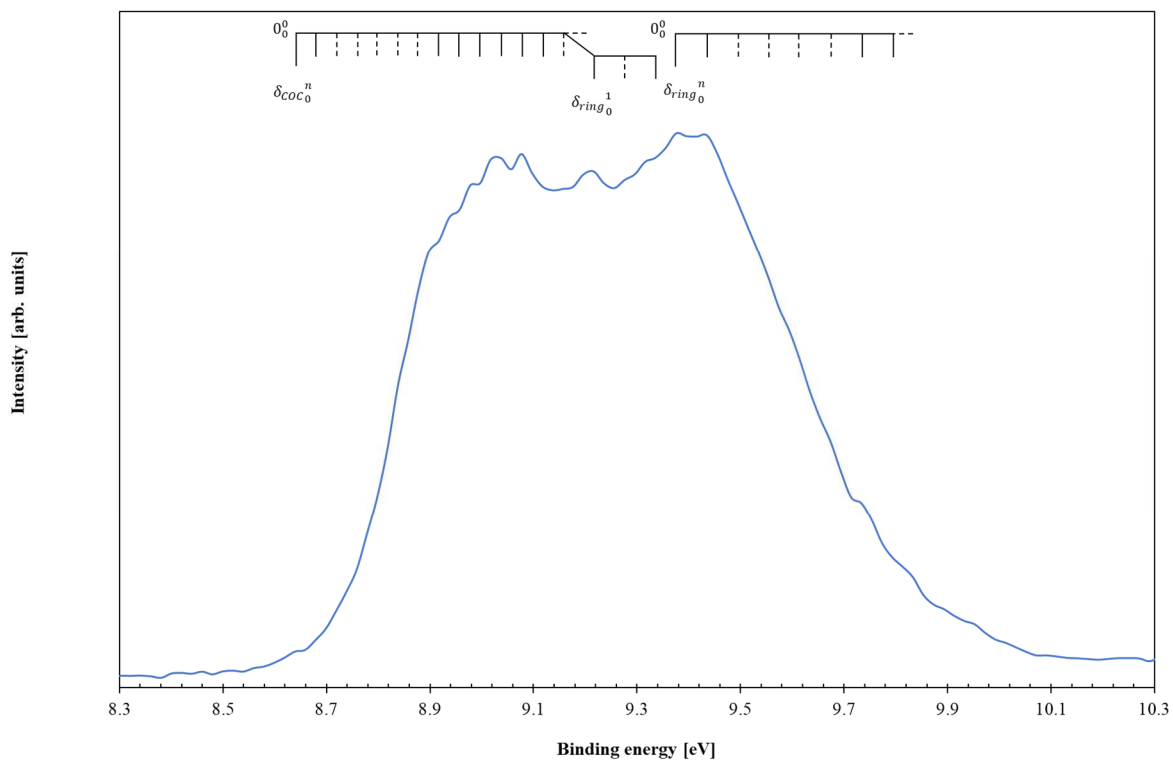


Fig. 6. Photoelectron bands of TCA,  $C_7H_5Cl_3O$ , in the 10.2–12.2 eV photon energy range. See text for further details.

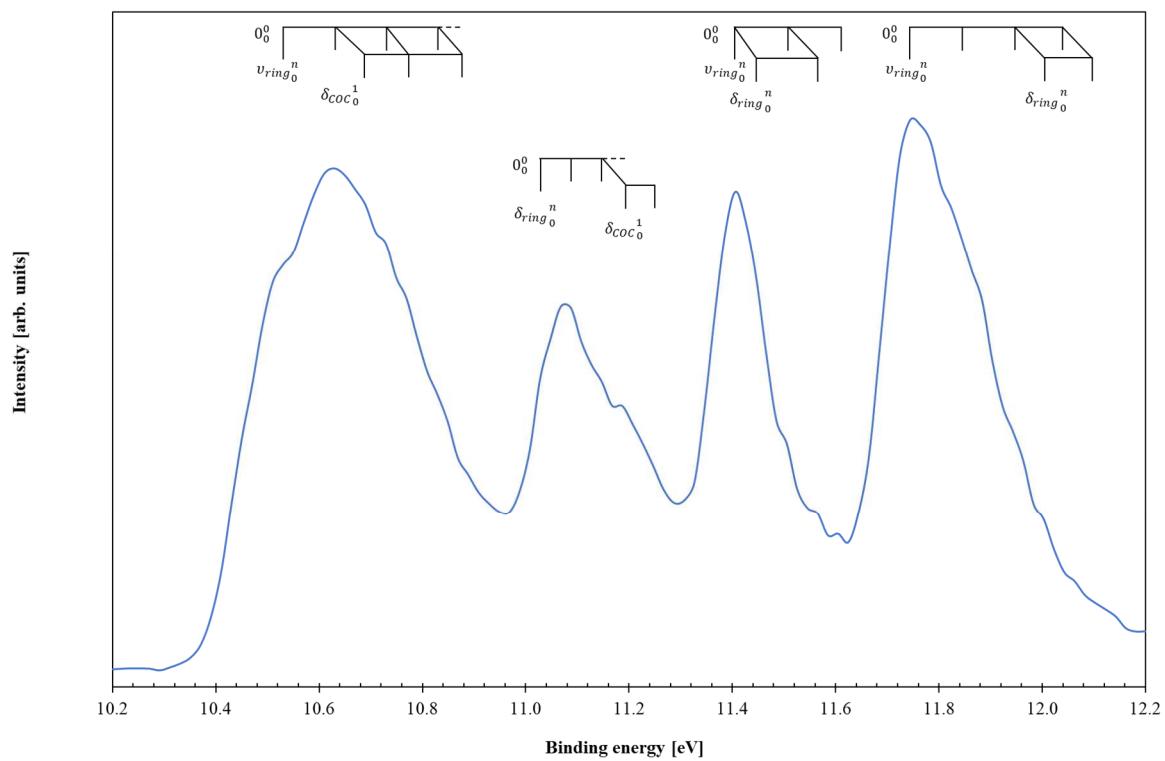


Table 1. Calculated vertical excitation energies (EOM-CCSD/aug-cc-pVTZ+R basis set) and oscillator strengths (singlet states) of TCA ( $C_7H_5Cl_3O$ ), compared with results from the present experimental data (all energies in eV). See details in text.

State	E (eV)	$f_L$	$\langle r^2 \rangle^a$	HOMO	HOMO-1	Other	Mixed Character	Exp. (eV) <sup>b</sup>	Cross-section (Mb)
				$3\pi$ (33a')	$2\pi$ (20a'')				
$\tilde{X}^1A'$	–	–	187						
$1^1A''$	4.880	0.00782	187				$3\pi(33a') \rightarrow 1\pi^*(21a'') + 2\pi(20a'') \rightarrow 2\pi^*(34a')$	4.319	2.90
$2^1A'$	6.043	0.00844	188				$3\pi(33a') \rightarrow 2\pi^*(34a') + 2\pi(20a'') \rightarrow 1\pi^*(21a'')$	5.55(0)	28.11
$3^1A'$	6.294	0.00106	200	$3\pi \rightarrow \sigma^*(CCl)(a')^c$					
$2^1A''$	6.491	0.00002	201		$2\pi \rightarrow \sigma^*(CCl)(a')^c$				
$4^1A'$	6.493	0.00932	220	$3\pi \rightarrow 4s\sigma(a')$				5.55(0)	28.11
$5^1A'$	6.713	0.75455	190				$3\pi(33a') \rightarrow 2\pi^*(34a') + 2\pi(20a'') \rightarrow 1\pi^*(21a'')$	6.262	166.87
$3^1A''$	6.771	0.51486	196				$3\pi(33a') \rightarrow 1\pi^*(21a'') + 2\pi(20a'') \rightarrow 2\pi^*(34a')$	6.262	166.87
$4^1A''$	6.810	0.10373	216		$2\pi \rightarrow 4s\sigma(a')$				
$6^1A'$	7.080	0.00337	260	$3\pi \rightarrow 4p\sigma(a')$					
$5^1A''$	7.099	0.00750	187			$\sigma(18a'') \rightarrow 2\pi^*(34a')$			
$7^1A'$	7.125	0.00520	249	$3\pi \rightarrow 4p\pi(a')$					
$6^1A''$	7.222	0.00401	276	$3\pi \rightarrow 4p\sigma(a'')$					
$8^1A'$	7.297	0.00510	190			$\sigma(18a'') \rightarrow 1\pi^*(21a'')$			
$9^1A'$	7.361	0.00406	230				$3\pi(33a') \rightarrow 3d\sigma(a') + 2\pi(20a'') \rightarrow 3d\pi(a'')$		
$10^1A'$	7.410	0.00022	265		$2\pi \rightarrow 4p\sigma(a'')$				
$7^1A''$	7.439	0.00954	255		$2\pi \rightarrow 4p\pi(a')$				
$11^1A'$	7.545	0.00367	317	$3\pi \rightarrow 3d\sigma(a')$					
$8^1A''$	7.560	0.00287	274	$3\pi \rightarrow 3d\sigma(a'')$					
$9^1A''$	7.681	0.00497	290		$2\pi \rightarrow 4p\sigma(a')$				
$12^1A'$	7.722	0.00155	291				$3\pi(33a') \rightarrow 3d\sigma(a') + 2\pi(20a'') \rightarrow 3d\sigma(a'')$		
$10^1A''$	7.758	0.01081	190			$1\pi(32a') \rightarrow 1\pi^*(21a'')$			
$13^1A'$	7.787	0.00035	225				$\sigma/n_{Cl}(19a'') \rightarrow 1\pi^*(21a'') + 3\pi(33a') \rightarrow 3d\pi(a')$		
$14^1A'$	7.796	0.00692	272				$3\pi(33a') \rightarrow 3d\pi(a') + \sigma/n_{Cl}(19a'') \rightarrow 1\pi^*(21a'')$		

11 <sup>1</sup> A''	7.826	0.00009	293		2π → 3dσ(a')			
12 <sup>1</sup> A''	7.889	0.01665	275			σ/n <sub>O</sub> (18a'') → 4sσ(a') + 3π(33a') → 3dπ(a'')		
13 <sup>1</sup> A''	7.899	0.00000	282			3π(33a') → 3dπ(a'') + σ/n <sub>O</sub> (18a'') → 4sσ(a')		
14 <sup>1</sup> A''	7.933	0.00320	182			σ/n <sub>O</sub> (18a'') → 1π*(21a'') + σ/n <sub>Cl</sub> (31a') → 2π*(34a')		
15 <sup>1</sup> A'	7.946	0.00801	400	3π → 3dσ(a')				
16 <sup>1</sup> A'	7.962	0.03470	209		1π(32a') → 2π*(34a')		7.64(4)	18.04
17 <sup>1</sup> A'	8.023	0.00532	334			3π(33a') → 5sσ(a') + 2π(20a'') → 3dσ(a'')		
15 <sup>1</sup> A''	8.008	0.00320	333		2π → 3dσ(a')			
16 <sup>1</sup> A''	8.053	0.00085	177			σ/n <sub>Cl</sub> (19a'') → 2π*(34a') + σ/n <sub>Cl</sub> (31a') → 1π*(21a'')		
17 <sup>1</sup> A''	8.064	0.00272	194			σ/n <sub>Cl</sub> (19a'') → 4sσ(a') + σ/n <sub>Cl</sub> (31a') → 4pσ(a'')		
18 <sup>1</sup> A'	8.080	0.00049	551	3π → 5pπ(a')				
19 <sup>1</sup> A'	8.127	0.00119	529	3π → 5pσ(a')				
18 <sup>1</sup> A''	8.131	0.00024	573	3π → 5pσ(a'')				
20 <sup>1</sup> A'	8.173	0.00082	333		2π → 3dπ(a'')			
19 <sup>1</sup> A''	8.175	0.00176	335		2π → 3dπ(a')			
21 <sup>1</sup> A'	8.216	0.03912	211			σ/n <sub>Cl</sub> (31a') → 4sσ(a') + σ/n <sub>Cl</sub> (19a'') → 3dσ(a'')	8.837	104.36
22 <sup>1</sup> A'	8.266	0.00034	695	3π → 6sσ(a')				
20 <sup>1</sup> A''	8.290	0.00333	358			3π(33a') → 3dσ(a') + 2π(20a'') → 5dσ(a'')		
23 <sup>1</sup> A'	8.365	0.00098	176			σ/n <sub>Cl</sub> (17a'') → 1π*(21a'') + σ/n <sub>Cl</sub> (31a') → 2π*(34a')		
24 <sup>1</sup> A'	8.401	0.00051	573		2π → 5pσ(a'')			
25 <sup>1</sup> A'	8.441	0.00071	380			2π(20a'') → 3dσ(a'') + 3π(33a') → 6pσ(a')		

<sup>a</sup> Mean value of  $r^2$  (electronic radial spatial extents)

<sup>b</sup> the last decimal on the energy value is given in brackets for these less-resolved features

<sup>c</sup> this valence MO ( $\sigma^*_{C-Cl}$ ) has the following shape:

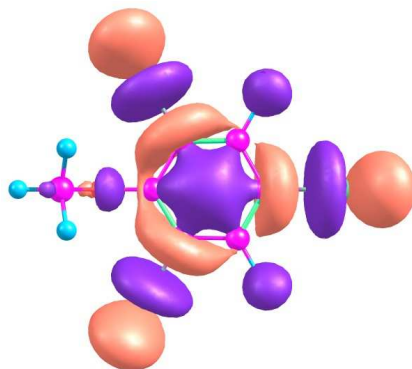


Table 2. Calculated valence and outer valence vertical ionisation energies and intensities (cc-pVTZ basis set at OVGf, P3/P3+ and EOMIP-CCSD/cc-pVTZ levels, CCSD/cc-pVTZ geometry) and experimental binding energies of TCA, C<sub>7</sub>H<sub>5</sub>Cl<sub>3</sub>O. For the sake of comparison, previous literature experimental values are also reported. All the energy values are in eV.

	33a <sup>-1</sup>	20a <sup>''-1</sup>	32a <sup>'-1</sup>	19a <sup>''-1</sup>	18a <sup>''-1</sup>	31a <sup>'-1</sup>	17a <sup>''-1</sup>	30a <sup>'-1</sup>	16a <sup>''-1</sup>	29a <sup>'-1</sup>
Koopmans' theorem	9.338	9.671	12.220	12.538	12.779	12.861	12.933	14.058	14.211	14.561
OVGF	8.791	9.127	11.204	11.477	11.156	11.817	11.899	12.937	13.057	13.340
Pole Strength	0.891	0.890	0.875	0.892	0.899	0.890	0.889	0.882	0.881	0.898
P3	9.315	9.601	11.165	11.368	11.079	11.686	11.729	12.843	13.007	13.237
Pole Strength	0.880	0.879	0.867	0.886	0.889	0.884	0.884	0.875	0.873	0.890
P3+	9.198	9.503	11.111	11.310	10.855	11.634	11.687	12.787	12.944	13.111
Pole Strength	0.876	0.876	0.867	0.884	0.882	0.883	0.883	0.874	0.872	0.887
EOMIP-CCSD	9.108	9.450	11.314	10.714	10.714	11.795	11.514	12.835	11.916	13.206
Exp. (this work)	9.08	9.38	11.09	10.63	–	11.41	11.74	12.74	–	13.00
Exp. Ref. [34]	8.90	–	–	10.65	11.11	11.40	11.78	–	–	–
Ref. [35]	8.69	–	–	–	–	–	–	–	–	–

	15a <sup>''-1</sup>	28a <sup>'-1</sup>	27a <sup>'-1</sup>	14a <sup>''-1</sup>	13a <sup>''-1</sup>	26a <sup>'-1</sup>	25a <sup>'-1</sup>	24a <sup>'-1</sup>	12a <sup>''-1</sup>	23a <sup>'-1</sup>	22a <sup>'-1</sup>	11a <sup>''-1</sup>	21a <sup>'-1</sup>
Koopmans' theorem	15.044	15.335	15.740	16.676	17.211	17.297	17.824	17.991	19.720	19.917	–	–	–
OVGF	13.646	13.978	14.085	15.007	15.414	15.681	16.097	16.209	17.210	17.861	–	–	–
Pole Strength	0.892	0.885	0.824	0.879	0.891	0.873	0.852	0.863	0.863	0.864	–	–	–
P3	13.856	14.200	14.159	15.240	15.512	15.836	16.213	16.311	17.511	17.948	–	–	–
Pole Strength	0.882	0.874	0.814	0.868	0.882	0.862	0.846	0.855	0.853	0.854	–	–	–
P3+	13.706	14.057	14.024	15.072	15.332	15.697	16.024	16.138	17.145	17.715	–	–	–
Pole Strength	0.877	0.870	0.814	0.862	0.876	0.858	0.843	0.851	0.839	0.847	–	–	–
EOMIP-CCSD	13.096	14.027	14.315	13.664	15.128	15.706	16.161	16.383	15.577	17.918	–	–	–
Exp. (this work)	13.42	13.91	–	14.89	15.35	–	–	16.10	16.90	17.40	19.15	22.05	23.19

Table 3. Proposed vibrational assignments in the 4.0–5.0 eV absorption band of TCA,  $C_7H_5Cl_3O$ . See text for further details.

Energy (eV)	Assignment*	$\Delta E(\delta_{ring})$ (eV) (out-of-plane)	$\Delta E(\nu_{CCl})$ (eV)	$\Delta E(\nu_{ring})$ (eV) (breathing)	$\Delta E(\delta_{CH})$ (eV)
4.226	$\nu_{CCl_1}^0$	–	0.093	–	–
4.319	$0_0^0$	–	–	–	–
4.38(9)(b,w)	$\delta_{ring_0}^1$	0.070	–	–	–
4.41(7)(s,b)	$\nu_{CCl_0}^1$	–	0.097	–	–
4.44(2)(b)	$\nu_{ring_0}^1$	–	–	0.122	–
4.45(2)(b)	$\delta_{ring_0}^2$	0.063	–	–	–
4.47(3)(s,w)	$\delta_{CH_0}^1$	–	–	–	0.153
4.51(2)(s)	$\nu_{CCl_0}^2$	–	0.095	–	–
4.55(8)(b)	$\nu_{ring_0}^2$	–	–	0.116	–
4.61(9)(s,w)	$\delta_{CH_0}^2$	–	–	–	0.146

(b) broad structure; (w) weak feature; (s) shoulder feature (the last decimal on the energy value is given in brackets for these less-resolved features).

\* Vibrational modes notation adopted from ref. [11]

Table 4. Proposed vibrational assignments and progressions in the 8.0–10.8 eV absorption band of TCA, C<sub>7</sub>H<sub>5</sub>Cl<sub>3</sub>O. See text for further details.

Energy (eV)	Assignment*	$\Delta E(\nu_{ring})$ (breathing) / $\Delta E(\nu_{CCl})$ (eV)	$\Delta E(\nu_{CH_3})$ (eV)
8.21(1)(b)	$\nu_{CH_3}^n$	–	–
8.46(9)(b,w)	$\nu_{CH_3}^{n+1}$	–	0.258
8.68(4)(s)	$\nu_{CH_3}^n$	–	–
8.93(3)(s)	$\nu_{CH_3}^{n+1}$	–	0.249
9.18(4)(s)	$\nu_{CH_3}^{n+2}$	–	0.251
9.42(9)(s,w)	$\nu_{CH_3}^{n+3}$	–	0.245
9.69(4)(s)	$\nu_{CH_3}^{n+4}$	–	0.265
8.837	$0_0^0$	–	–
8.93(3)(s)	$\nu_{ring_0^1} / \nu_{Ccl_0^1}$	0.096	–
9.07(7)(s,w)	$\nu_{CH_3_0^1}$	–	0.240
9.18(4)(s)	$\nu_{ring_0^1} / \nu_{Ccl_0^1} + \nu_{CH_3_0^1}$	–	0.251
9.308	$\nu_{ring_0^2} / \nu_{Ccl_0^2} + \nu_{CH_3_0^1}$	0.124	–
9.34(3)(s,w)	$\nu_{CH_3_0^2}$	–	0.266
9.42(9)(s,w)	$\nu_{ring_0^1} / \nu_{Ccl_0^1} + \nu_{CH_3_0^2}$	–	0.245
9.523	$\nu_{ring_0^2} / \nu_{Ccl_0^2} + \nu_{CH_3_0^2}$	–	0.215
9.60(4)(s)	$\nu_{CH_3_0^3}$	–	0.261
9.69(4)(s)	$\nu_{ring_0^1} / \nu_{Ccl_0^1} + \nu_{CH_3_0^3}$	–	0.265
10.01(5)(s)	–	–	–
10.129	$\nu_{ring_0^1} / \nu_{Ccl_0^1}$	0.114	–
10.26(4)(s)	$\nu_{CH_3_0^1}$	–	0.249
10.332	$\nu_{ring_0^1} / \nu_{Ccl_0^1} + \nu_{CH_3_0^1}$	–	–
10.43(6)(s)	$\nu_{ring_0^2} / \nu_{Ccl_0^2} + \nu_{CH_3_0^1}$	0.104	–
10.507	$\nu_{CH_3_0^2}$	–	0.243
10.59(7)(s)	$\nu_{ring_0^1} / \nu_{Ccl_0^1} + \nu_{CH_3_0^2} / \nu_{ring_0^1}$	0.091	–

(b) broad structure; (w) weak feature; (s) shoulder feature (the last decimal on the energy value is given in brackets for these less-resolved features).

\* Vibrational modes notation adopted from ref. [11]

Table 5. Proposed vibrational assignments in the 8.0–10.0 eV photoelectron band of TCA,  $C_7H_5Cl_3O$ . See text for further details.

Energy (eV)	Assignment*	$\Delta E(\delta_{COC})$ (eV)	$\Delta E(\delta_{ring})$ (eV) (out-of-plane)
8.6(5)(b)	$0_0^0$	–	–
8.6(8)(s)	$\delta_{COC}_0^1$	0.030	–
8.7(2)(s,w)	$\delta_{COC}_0^2$	0.040	–
8.7(6) (s,w)	$\delta_{COC}_0^3$	0.040	–
8.8(0) (s,w)	$\delta_{COC}_0^4$	0.040	–
8.8(4)(s,w)	$\delta_{COC}_0^5$	0.040	–
8.8(8)(s,w)	$\delta_{COC}_0^6$	0.040	–
8.9(2)(s)	$\delta_{COC}_0^7$	0.040	–
8.9(6)(s)	$\delta_{COC}_0^8$	0.040	–
9.0(0)(s)	$\delta_{COC}_0^9$	0.040	–
9.0(4)(b)	$\delta_{COC}_0^{10}$	0.040	–
9.08	$\delta_{COC}_0^{11}$	0.040	–
9.1(2)(s)	$\delta_{COC}_0^{12}$	0.040	–
9.1(6)(w)	$\delta_{COC}_0^{13}$	0.040	–
9.22	$\delta_{COC}_0^{13} + \delta_{ring}_0^1$	–	0.060
9.2(8)(s)	$\delta_{COC}_0^{13} + \delta_{ring}_0^2$	–	0.060
9.3(4)(s)	$\delta_{COC}_0^{13} + \delta_{ring}_0^3$	–	0.060
9.38	$0_0^0$	–	–
9.44	$\delta_{ring}^1$	–	0.060
9.5(0)(s,w)	$\delta_{ring}^2$	–	0.060
9.5(6)(s)	$\delta_{ring}^3$	–	0.060
9.6(2)(s)	$\delta_{ring}^4$	–	0.060
9.6(7)(s)	$\delta_{ring}^5$	–	0.059
9.7(4)(s)	$\delta_{ring}^6$	–	0.070
9.7(9)(s)	$\delta_{ring}^7$	–	0.050

(b) broad structure; (s) shoulder feature; (w) weak feature (the last decimal on the energy value is given in brackets for these less-resolved features).

\* Vibrational modes notation adopted from ref. [11]

Table 6. Proposed vibrational assignments in the 10.2–12.2 eV photoelectron band of TCA,  $C_7H_5Cl_3O$ . See text for further details.

Energy (eV)	Assignment*	$\Delta E(\nu_{ring})$ (breathing) / $\Delta E(\nu_{CCl})$ (eV)	$\Delta E(\delta_{ring})$ (eV) (out-of-plane)	$\Delta E(\delta_{COC})$ (eV)
10.5(3)(s)	$0_0^0$	–	–	–
10.63	$\nu_{ring_0^1}/\nu_{CCl_0^1}$	0.100	–	–
10.6(7)(s)	$\nu_{ring_0^1}/\nu_{CCl_0^1} + \delta_{COC_0^1}$	–	–	0.040
10.7(3)(s)	$\nu_{ring_0^2}/\nu_{CCl_0^2}$	0.100	–	–
10.7(7)(s)	$\nu_{ring_0^2}/\nu_{CCl_0^2} + \delta_{COC_0^1}$	–	–	0.040
10.8(3)(s)	$\nu_{ring_0^3}/\nu_{CCl_0^3}$	0.100	–	–
10.8(7)(s)	$\nu_{ring_0^3}/\nu_{CCl_0^3} + \delta_{COC_0^1}$	–	–	0.040
11.0(3)(s)	$0_0^0$	–	–	–
11.09	$\delta_{ring_0^1}$	–	0.060	–
11.1(5)(s)	$\delta_{ring_0^2}$	–	0.060	–
11.19	$\delta_{ring_0^2} + \delta_{COC_0^1}$	–	–	0.040
11.2(5)(s)	$\delta_{ring_0^3} + \delta_{COC_0^1}$	–	0.060	–
11.41	$0_0^0$	–	–	–
11.4(5)(s)	$\delta_{COC_0^1}$	–	–	0.040
11.5(1)(s)	$\nu_{ring_0^1}/\nu_{CCl_0^1}$	0.100	–	–
11.5(7)(s,b)	$\nu_{ring_0^1}/\nu_{CCl_0^1} + \delta_{ring_0^1}$	–	0.060	–
11.61	$\nu_{ring_0^2}/\nu_{CCl_0^2}$	0.100	–	–
11.74	$0_0^0$	–	–	–
11.8(4)(s)	$\nu_{ring_0^1}/\nu_{CCl_0^1}$	0.100	–	–
11.9(4)(s)	$\nu_{ring_0^2}/\nu_{CCl_0^2}$	0.100	–	–
12.0(0)(s)	$\nu_{ring_0^2}/\nu_{CCl_0^2} + \delta_{ring_0^1}$	–	0.060	–
12.0(4)(s,w)	$\nu_{ring_0^3}/\nu_{CCl_0^3}$	0.100	–	–
12.1(0)(s,w)	$\nu_{ring_0^3}/\nu_{CCl_0^3} + \delta_{ring_0^1}$	–	0.060	–

(b) broad structure; (s) shoulder feature; (w) weak feature (the last decimal on the energy value is given in brackets for these less-resolved features).

\* Vibrational modes notation adopted from ref. [11]

Table 7. Energy value (eV), quantum defect ( $\delta$ ) and assignment of the Rydberg series converging to the ionic electronic ground ( $33a'^{-1}$ ), first ( $20a''^{-1}$ ), second ( $32a'^{-1}$ ) and third ( $19a''^{-1}$ ) excited states of TCA,  $C_7H_5Cl_3O$ .

$E_n$	$\delta$	assignment	$E_n$	$\delta$	assignment
<b>IE<sub>1</sub> = 9.08 eV (<math>33a'</math>)<sup>-1</sup></b>			<b>IE<sub>3</sub> = 11.09 eV (<math>32a'</math>)<sup>-1</sup></b>		
<i>(nsa' ← 33a')</i>			<i>(nsa' ← 32a')</i>		
5.55(0)(b)	2.04	4s $\sigma$	7.64(4)(b)	2.01	4s $\sigma$
7.64(4)(b)	1.92	5s $\sigma$	9.523	2.05	5s $\sigma$
8.21(1)(b)	2.04	6s $\sigma$	10.26(4)(s)	1.93	6s $\sigma$
<i>(np ← 33a')</i>			<i>(np ← 32a')</i>		
6.262	1.80	4p	8.46(9)(b,w)	1.72	4p
<i>(nd ← 33a')</i>			9.69(4)(s)	1.87	5p
7.64(4)(b)	-0.08	3d	10.332	1.75	6p
8.21(1)(b)	0.04	4d	10.59(7)(s)	1.73	7p
<b>IE<sub>2</sub> = 9.38 eV (<math>20a''</math>)<sup>-1</sup></b>			<i>(nd ← 32a')</i>		
<i>(nsa' ← 20a'')</i>			9.42(9)(s,w)	0.13	3d
6.262	1.91	4s $\sigma$	10.129	0.23	4d
–	–	5s $\sigma$	10.507	0.16	5d
8.46(9)(b,w)	2.13	6s $\sigma$	<b>IE<sub>4</sub> = 10.63 eV (<math>19a''</math>)<sup>-1</sup></b>		
<i>(np ← 20a'')</i>			<i>(nsa' ← 19a'')</i>		
7.64(4)(b)	1.19	4p	7.64(4)(b)	1.86	4s $\sigma$
8.46(9)(b,w)	1.13	5p	9.18(4)(s)	1.93	5s $\sigma$
8.68(4)(s)	1.56	6p	<i>(np ← 19a'')</i>		
8.93(3)(s)	1.45	7p	8.837	1.24	4p
<i>(nd ← 20a'')</i>			9.69(4)(s)	1.18	5p
7.64(4)(b)	0.19	3d	10.01(5)(s)	1.29	6p
8.46(9)(b,w)	0.12	4d	<i>(nd ← 19a'')</i>		
			8.93(3)(s)	0.17	3d
			9.69(4)(s)	0.18	4d

<sup>a</sup> (b) broad feature; (w) weak structure; (s) shoulder structure (the last decimal on the energy value is given in brackets for these less-resolved features).